Solution Grown Ternary Semiconductors: Nanostructuring and Stereoelectronic Lone Pair Distortions in I-V-VI$_2$ Materials

Alan Medina-Gonzalez,[1,‡] Philip Yox,[1,2,‡] Yunhua Chen,[1,2] Marquix A. S. Adamson,[1] Bryan A. Rosales,[1] Maranny Svay,[1] Emily A. Smith,[1,2] Richard D. Schaller,[3,4] Kui Wu,[5] Aaron J. Rossini,[1,2] Kirill Kovnir,*[,1,2] Javier Vela*[,1,2]

[1]Department of Chemistry, Iowa State University, Ames, Iowa, 50011, United States. [2]US DOE Ames Laboratory, Ames, Iowa, 50011, United States. [3]Department of Chemistry, Northwestern University, Evanston, Illinois, 60208, United States. [4]Center for Nanoscale Materials, US DOE Argonne National Laboratory, Lemont, Illinois, 60439, United States. [5]College of Chemistry and Environmental Science, Hebei University, Baoding City, Hebei Province, 071002, China.

ABSTRACT: Alkali pnictogen dichalcogenides—I-V-VI$_2$ or APnCh$_2$—have been identified as promising semiconducting materials for energy conversion devices. However, the controlled nanoscale synthesis and our understanding of the effects of cation ordering and stereochemically active lone pairs on the structures of these ternary compounds remain underdeveloped. Here, we use solution phase chemistry to synthesize a family of APnCh$_2$ materials, including LiSbSe$_2$, NaSbS$_2$, NaSbSe$_2$, NaBiS$_2$, and NaBiSe$_2$. Our approach utilizes alkali metal hydrides (AH) or carboxylates, A(O$_2$CR), PnPh$_3$, and elemental chalcogens as synthetic precursors, and oleylamine or 1-octadecene as solvents. Synthetic manipulation *via* fine-tuning of reaction temperature enables control over the degree of ordering caused by the Sb 5s^2 lone pair-induced distortions in NaSbS$_2$. Pair distribution function (PDF) analysis demonstrates the structure of the Sb-containing phases deviates much more from a disordered rock salt structure than that of the Bi-containing phases. This local distortion, induced by the Sb lone pair, leads to a previously unreported non-centrosymmetric NaSbS$_2$ crystal structure, which is additionally supported by second harmonic generation (SHG). Infrared and multinuclear solid-state NMR spectroscopies show that oleylamine or chelating carboxylates and, in some cases, unreacted precursors (LiH and PnPh$_3$) remain bound to the nanocrystalline surfaces. A deeper understanding of the local atomic environment, long range ordering, surface chemistry, and optoelectronic properties of these materials which may speed up their fundamental study and application.

INTRODUCTION

Ternary alkali pnictogen dichalcogenides have been identified as promising semiconductors for energy conversion devices. The parent structure of this family of compounds is similar to that of rock salt PbTe, which has been at the forefront of thermoelectric applications for over a decade.[1–4] Replacing Pb^{2+} with a combination of Ag$^+$ and Sb^{3+} results in ternary AgSbTe$_2$, which exhibits a cation-disordered rock-salt structure (Figure 1a). Both AgSbTe$_2$ and AgSbSe$_2$ ternaries are excellent thermoelectrics,[5–16] and their performance can be further improved by nanostructuring and doping.[3,4,17,18] A high ZT of 2.6 was recently reported for Cd-doped AgSbTe$_2$.[19]

Other ternary rock salt I-V-VI$_2$ semiconductors with formula APnCh$_2$ (A = Li, Na, K, Rb, Ag; Pn = As, Sb, Bi; Ch = S, Se, Te) are thought to also exhibit cation-disordered rock-salt structures, with the monovalent cation and pnictogen atoms occupying the same Wyckoff position.[20–24] However, a majority of studies to date have focused on ternary rock-salt compounds based on Ag, with much fewer reports available for those based on alkali metals. This may be due to the unique challenges associated with working with these materials—for example, the high reactivity of the reduced forms of the alkali metals that are often used as precursors during

higher temperature syntheses, or the high mobility of the alkali cations in the final ternary compounds.
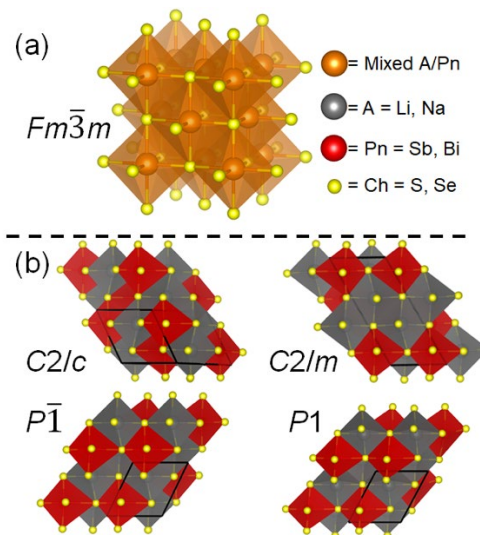

Figure 1. (a) Mixed cation rock salt structure of ternary APnCh$_2$ semiconductors (A = Li, Na; Pn = Sb, Bi; Ch = S, Se), and (b) cation ordered polymorphs of NaSbS$_2$ (Monoclinic $C2/c$ and $C2/m$, and triclinic $P\bar{1}$ and $P1$).

Several computational studies have been performed to assess the potential utility of $NaSbS_2$ and other $APnCh_2$ compounds in photovoltaic and thermoelectric devices.[25–27] According to theory, $NaSbS_2$ may have a large absorption coefficient and a band gap that is optimal for photovoltaic solar cells.[25–31] $NaSbS_2$ has also been theorized to have a high dielectric constant, carrier effective masses that are favorable for transport, and a band gap suitable for thermoelectrics.[25,32] Further, $NaSbS_2$ is made of Earth-abundant and relatively non-toxic, biocompatible elements, making it an ideal candidate in multiple applications. Nonetheless, a majority of literature $APnCh_2$ preparations use spray pyrolysis or other high temperature methods, which can result in aggregated particles containing, in some cases, unreacted precursors.[27,33]

Despite multiple studies performed to date, the exact crystal structure of $NaSbS_2$ remains unclear. The earliest experimental reports suggest that $NaSbS_2$ adopts a cation-disordered rock salt ($Fm\overline{3}m$) structure.[27–29,34–36] However, computations show that other, cation-ordered monoclinic $C2/c$, $C2/m$, and triclinic $P\overline{1}$ structures have relatively similar energies and are therefore also reasonable for this material (Figure 1b). In addition to cation-ordering, local distortions caused by the presence of stereoactive lone pairs on the pnictogen atom further complicate structural characterization. For example, pair distribution function analysis of $AgBiS_2$ revealed off-

centering of the Bi atoms, presumably caused by the $6s^2$ lone pair.[37] In the case of Sb, the more stereochemically active $5s^2$ lone pair should lead to even greater distortions. Small substitutions of Sb into $AgBiSe_2$ did not result in any significant distortions but more recently, $AgSbSe_2$ was reported to have Sb off-centering in the $\langle 100 \rangle$ direction.[38,39] The analog arsenic compounds $LiAsSe_2$ and $NaAsCh_2$ displayed local geometries that strongly deviate from the idealized rock salt structure.[40,41]

In this study, we describe a general solution phase synthesis of a wide family of alkali metal based $APnCh_2$ compounds, including $LiSbSe_2$, $NaSbS_2$, $NaSbSe_2$, $NaBiS_2$, and $NaBiSe_2$. We resort to pair distribution function (PDF) analysis to determine the presence and extent of local and long-range order across these family of materials. Our studies pinpoint the importance of the stereoelectronic Pn lone pair in dictating local and long-range ordering. In addition, we employ electron localization function (ELF) to visualize the lone pair in real space. Finally, the surface chemistry of $I-V-VI_2$ nanocrystals is assessed by a combination of thermal analysis, as well as by vibrational and solid-state NMR spectroscopies. We hope that these studies will enable more predictive syntheses as well as fundamental spectroscopic and applied studies of technologically relevant ternary $I-V-VI_2$ semiconductors.

Table 1. Solution phase synthesis of nanocrystalline $APnCh_2$ (A = Li, Na; Pn = Sb, Bi; E = S, Se).[a]

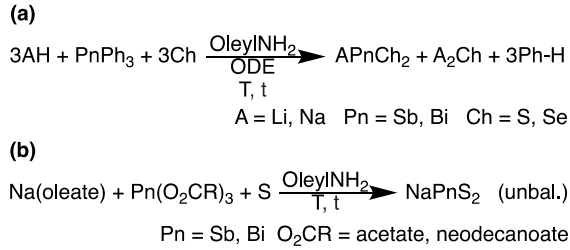| #	A + Pn Precursors	Ch Precursor	Solvent	T /°C	t /min	Product(s) (space group,[b] %)	Size (nm)[c]
1	$LiH + SbPh_3$	Se	$OleylNH_2$/ODE	290	1	**$LiSbSe_2$** ($P1$, 100)	220±90
2	$Na(oleate) + Sb(OAc)_3$	S	$OleylNH_2$	150	30	**$NaSbS_2$** ($Fm\overline{3}m$, 85), Sb_2O_3 (15)	38±15
3	$Na(oleate) + Sb(OAc)_3$	S	$OleylNH_2$	200	30	**$NaSbS_2$** ($Fm\overline{3}m$, 100)	38±20
4	$Na(oleate) + Sb(OAc)_3$	S	$OleylNH_2$	250	30	**$NaSbS_2$** ($Fm\overline{3}m$, 95; $P1$, 5)	34±12
5	$Na(oleate) + Sb(OAc)_3$	S	$OleylNH_2$	300	30	**$NaSbS_2$** ($P1$, ≥90)	35±21
6	$Na(oleate) + Sb(NMe_2)_3$	S	$OleylNH_2$	200	5	Amorphous	-
7	$Na(oleate) + Sb(OAc)_3$	Se	$OleylNH_2$/ODE	170	30	Sb_2O_3 (100)	45±29
8	$NaH + SbPh_3$	Se	$OleylNH_2$/ODE	300	10	**$NaSbSe_2$** ($P1$, 100)	145±70
9	$Na(oleate) + Bi(neodecanoate)_3$	S	$OlelyNH_2$	180	60	**$NaBiS_2$** ($Fm\overline{3}m$, 100)[50]	10±2
10	$NaH + BiPh_3$	Se	$OleylNH_2$/ODE	180	120	**$NaBiSe_2$** ($Fm\overline{3}m$, 100)	44±22

[a]$[A]_o = [Pn]_o = [Ch]_o/2 = 0.023M$ (see Methods). [b]The presence of quotation marks indicates that the structure (space group) apparent by powder XRD data is NOT supported by PDF analysis (see text). [c]Single crystalline domain (Scherrer) size of major crystalline phase (nm).

RESULTS AND DISCUSSION

Synthesis and Evolution of Ternary $APnCh_2$ Phases. (A = Li, Na; Pn = Sb, Bi; Ch = S, Se) Alkali metal hydrides are quickly becoming versatile synthetic precursors for the synthesis of multinary semiconductors. Recent examples include the high temperature synthesis of bulk (polycrystalline) AZnSb (A = Na, K)[42–45] and $Ba_{1-x}K_xFe_2As_2$,[46] as well as the solution phase synthesis of nanocrystalline $LiZnP$,[47] $LiZnSb$,[48] $NaCd_4P_3$,[49] and $NaBiS_2$.[50] Building on these successes, we find that heating a mixture of AH (A = Li, Na), Ph_3Pn (Pn = Sb, Bi), and Se in 1-octadecene (ODE) and oleylamine (oleylNH_2) is a convenient method to prepare nanocrystalline $LiSbSe_2$, $NaSbSe_2$, and $NaBiSe_2$ (Scheme 1a and Table 1).

Powder X-ray diffraction (XRD) patterns of these ternary diselenides show reflections consistent with a mixed-cation, rock salt structure ($Fm\overline{3}m$)—see Supporting Information (SI). From the corrected widths of the major reflections in each case, we calculate average single crystalline domains or Scherrer sizes of 220±90 nm for $LiSbSe_2$, 145±70 nm for $NaSbSe_2$, and 44±22 nm for $NaBiSe_2$. Interestingly, the temperatures required to prepare the Sb-based ternaries (290–300 °C) are generally higher than those required to prepare Bi-based ternaries (180 °C). This implies that the reduction of Ph_3Sb into intermediate Sb^o seeds, and their subsequent reaction with alkali and chalcogen precursors requires more energy compared to that of Ph_3Bi.[48,50]

Scheme 1. Solution phase synthesis of $APnCh_2$ (I-V-VI$_2$) semiconductors (see SI).

(a)

$$3AH + PnPh_3 + 3Ch \xrightarrow[\text{ODE}]{\text{OleyINH}_2} APnCh_2 + A_2Ch + 3Ph\text{-}H$$
$$T, t$$

$$A = Li, Na \quad Pn = Sb, Bi \quad Ch = S, Se$$

(b)

$$Na(\text{oleate}) + Pn(O_2CR)_3 + S \xrightarrow[\text{T, t}]{\text{OleyINH}_2} NaPnS_2 \quad (\text{unbal.})$$

$$Pn = Sb, Bi \quad O_2CR = \text{acetate, neodecanoate}$$

Using a modified version of this solution phase approach—starting from readily available sodium oleate, antimony acetate, and sulfur in oleylamine—one can also prepare nanocrystalline $NaSbS_2$ (Scheme 1b and Figure 2). This reaction is particularly temperature dependent. The powder XRD of solids isolated from the reaction at 100 °C only shows small 44±23 nm Sb_2O_3 particles. This is likely a result of post-synthetic exposure to air and consequent oxidation of the aforementioned Sb seeds. (Note: the oleylamine solvent, present in excess relative to all other precursors and reactants, acts as a mild reducing agent.)[51,52] When the reaction is carried out at 150 °C or 200 °C, powder XRD suggests the formation of $NaSbS_2$ with a disordered, mixed-cation rock salt structure ($Fm\bar{3}m$). Nanocrystals synthesized at 300 °C (35±21 nm) have similar Scherrer sizes as those synthesized at 200 °C (38±20 nm). However, increasing the temperature to 250 or 300 °C results in additional peaks at ~15 2θ. These peaks are not from admixtures and indicate a deviation from the rock-salt structure—see PDF analysis below. Conclusive determination of the crystal structure was not possible from a simple comparison between the powder XRD patterns to those of the theoretical $C2/c$, $C2/m$, $P\bar{1}$, and $P1$ structures alone.
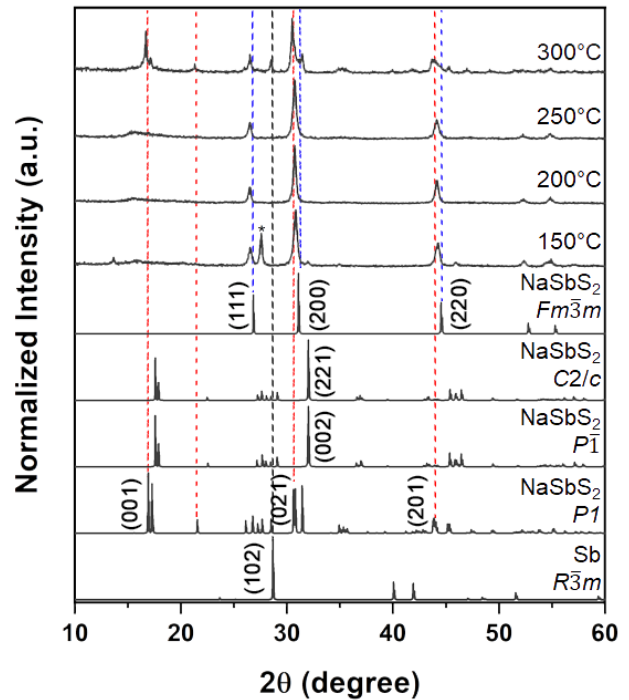

Figure 2. Powder XRD of solids isolated after 30 min reaction between Na(oleate), Sb(OAc)$_3$, and sulfur in oleylamine at different temperatures (see Table 1). Standard patterns of $NaSbS_2$ ($Fm\bar{3}m$, 60285), $NaSbS_2$ ($C2/c$, 43909), $NaSbS_2$ ($P\bar{1}$, 200597), $NaSbS_2$ ($P1$, from PDF refinement below), Sb_2O_3 ($Fd\bar{3}m$, 9007609), and Sb metal ($R\bar{3}m$, 161493) shown for comparison. Reaction at 150 °C also formed Sb_2O_3 (*).

Pair Distribution Function Analysis. In the ideal rock-salt structure type of I-V-VI$_2$ materials, the alkali metal and pnictogen occupy the same crystallographic site. This statistical occupancy limits the utility of traditional X-ray diffraction data, creating challenges to fully understand a material's structure or predict its properties. In this case, pair distribution function (PDF) analysis, a total scattering technique that utilizes both Bragg and diffuse scattering, is an ideal tool for observing the local structure of the material.[53] Using PDF of X-ray total scattering data collected at the 11-ID-B beamline of the Advanced Photon Source at Argonne National Laboratory, we find that the local structures of certain materials within the I-V-VI$_2$ family significantly deviate from the idealized rock salt structure. This is particularly the case for samples containing Sb.

In the case of $NaSbS_2$, multiple phases including ideal and distorted rock salt structures have been reported. Here, we considered the models corresponding to the noncentrosymmetric space groups $P1$ (triclinic), Cc, Cm (both monoclinic), and centrosymmetric space groups $C2/c$, $C2/m$ (both monoclinic), and $Fm\bar{3}m$ (rock salt) (Figure 1). The choice to include noncentrosymmetric space groups as possible solutions stems from the compositionally relevant materials $LiAsSe_2$[40] and $NaAsS_2$[41] which are reported to be noncentrosymmetric and exhibit a phenomenon exclusive to

noncentrosymmetric materials: second harmonic generation (SHG). To the best of our knowledge, only centrosymmetric crystal structures have been reported for NaSbS$_2$.

To obtain the $P1$, Cc, and Cm models, we simply removed the appropriate symmetry restrictions from the centrosymmetric $P\overline{1}$, $C2/c$, and $C2/m$, respectively. We started our analysis with the nanocrystalline NaSbS$_2$ synthesized at 300 °C (see Figure 2 and Table 1), by first fitting the data from 2.15 Å to 10.0 Å. In this range $P1$, Cc, and $C2/c$ are clearly superior to Cm, $C2/m$ and $Fm\overline{3}m$. Because the $Fm\overline{3}m$ only gives a fit of $R_w > 0.4$, we did not further attempt to fit cubic supercell structures. The $P1$, Cc, and $C2/c$ models provide remarkably good fits after refinement, with R_w = 0.09, 0.14, and 0.14, respectively (Figure 3). Furthermore, this analysis is in good agreement with $P\overline{1}$ and $C2/c$ structures having the lowest total energies, as computed from VASP (see SI). Once the best fitting was obtained from 2.15 Å to 10.0 Å, the range was increased to 20.0 Å. Refinement in this range makes it apparent that $P1$ is a reasonable yet somewhat inexact model, with some discrepancies toward 17-19 Å (Figure 3).

The difference between $P1$ and $C2/c$ stems from the symmetry restrictions placed upon the Sb and Na atoms in $C2/c$. The volumes for the primitive part of the unit cell for $P\overline{1}$ and $C2/c$ models are similar, but due to its higher symmetry, $C2/c$ has less than half of the refinement parameters due to the Na and Sb located in special positions with fixed x and z coordinates. Moving to Cc from $C2/c$ increases the number of parameters refined which is expected to help the refinement. However, while Sb and Na no longer have fixed x and z coordinates, the 4 Sb atoms still have restrictions on their positions relative to each other making the resulting refinement only marginally better.To determine if the noncentrosymmetric structures derived from PDF refinements were reasonable or just over-parameterizations of the data, a sample of NaSbS$_2$ was tested for SHG activity (SI). Indeed, SHG activity was detected, in agreement with the noncentrosymmetric nature of the crystal structure. The combination of PDF and SHG activity point to P1 as the real symmetry of the "high temperature" NaSbS$_2$ phase.
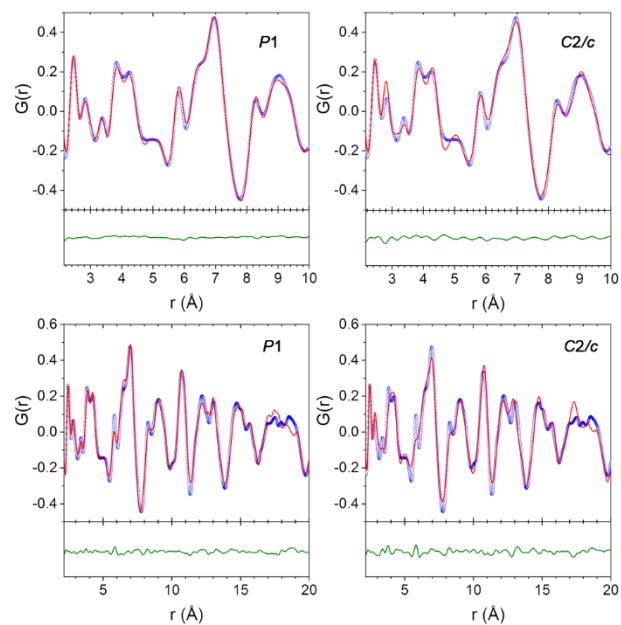

Figure 3. PDF function plots for $P1$ and $C2/c$ structures of high temperature (300 °C) solution grown NaSbS$_2$ between 2-10 Å (top) and 2-20 Å (below). Experimental and $P1$ (left) or $C2/c$ (right) model data are shown in blue and red, respectively. The difference curve of G(r) between the model and the experimental data is shown at the bottom in green.

In comparison to the high temperature phase, PDF analysis of the lower temperature NaSbS$_2$ nanocrystals—made between 200–250 °C—shows a greatly reduced peak at 2.8 Å. While the 2.2 Å to 8 Å region of these data sets fit reasonably well with a modified $P1$ model, the remaining 8 Å to 30 Å region was fit with the rock salt ($Fm\overline{3}m$) model. A comparison of the NaSbS$_2$ nanocrystals synthesized at 200, 250, and 300 °C is shown in the SI. In agreement with powder XRD, the fit to the cubic pattern gets worse with increasing synthetic temperature. From the PDF, it is apparent that distortions occur even at lower synthetic temperatures; however, they lack long range ordering—past 8 Å—so that the average structure remains cubic. In contrast to the multiple structures reported and discussed for NaSbS$_2$, the presence of distortions in LiSbSe$_2$ and NaSbSe$_2$ remains undocumented. To date, these materials have only been reported and assumed to adopt ideal, undistorted rock-salt $Fm\overline{3}m$ structures. Nonetheless, PDF analysis shows otherwise (Figure 4). In the ideal structure, NaSbSe$_2$ has six equivalent Sb-Se bond distances of ~2.98 Å. This is inconsistent with other Sb-Se bond distances such as those in Sb$_2$Se$_3$, which range from 2.59–2.80 Å.[54] In the PDF, the first intense peak representing the nearest neighbor Sb-Se distance is located at 2.65 Å.
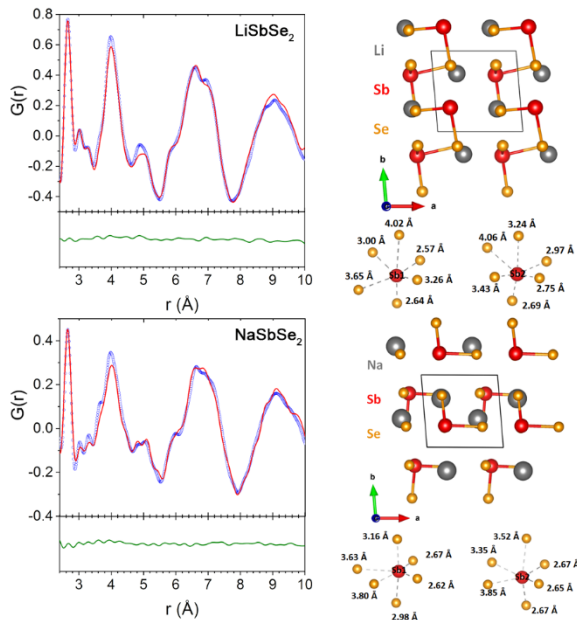
Figure 4. PDF function plots of solution grown LiSbSe$_2$ and NaSbSe$_2$ (left). Experimental and $P1$ model data are shown in blue and red, respectively. The difference curve of G(r) between the model and the experimental data is shown at the bottom in green. Coordination environments of Sb(1) and Sb(2) and (As-Se) interactions in each compound (right).

Refinement with a rock-salt structure was unsuccessful. Instead, following a similar approach to that reported for LiAsSe$_2$,[40] a primitive cell of the smallest repeating fragment with all symmetry unconstrained was used for refinement. (Note: due to Li being a very light element with a small scattering factor, Li was fixed in its position to avoid any unrealistic bond lengths). Fitted to the 2.4 Å to 10 Å region, this resulted in robust R_w values of 0.11 and 0.15 for LiSbSe$_2$ and NaSbSe$_2$, respectively (Figure 4). Further refinement with these models to higher r distances was unsuccessful. The disagreement at higher r distances could possibly arise from the inability of such a small unit cell to accurately describe long-range order. However, attempts to use a supercell with different Se coordination were also unsuccessful. Another explanation of the inability to fit the > 10 Å region is that the local distortions are not correlated and that only the average structure is observed in this range. This is consistent with the PXRD which shows a diffraction pattern than can be indexed as a rock-salt $Fm\bar{3}m$ structure (see Supporting Information). Regardless, vital information about the coordination of the Sb atoms can be extracted from the PDF analysis. Most importantly, Sb has 3 short distances and 3 long distances (Figure 4). In other words, the coordination of Sb is more like that of As in LiAsSe$_2$[40] and vastly different from the coordination of Bi in NaBiSe$_2$ (see below).

PDF analysis of the Bi-containing ternaries shows a much simpler picture than that for the Sb-containing materials. From 2 Å to 30 Å (Figure 5), both NaBiS$_2$ and NaBiSe$_2$ give a good fit to the cubic model ($Fm\bar{3}m$), with

R_w values of 0.18 and 0.11, respectively. These results show that the basic cation disordered, rock salt model with a statistical occupation of Na and Bi describes the real structure quite well. However, carefully analyzing the first peak at ~2.8 Å—corresponding to nearest neighbor Bi-Se/S—shows that the fit is imperfect. While the calculated pattern provides significant overlap with the raw data, the shape of this early peak is asymmetric and splits into two, with one peak at lower r value. Attempts to refine the Bi positions without symmetry constraints failed to give better agreement with the data. At present, we hypothesize that this small peak asymmetry could be due to a very small degree of lone pair-induced distortion, as suggested previously.[37] Bi^{3+} 6s^2 lone pair have been reported to be stereoactive in Bi$_2$WO$_6$ and AgBiCh$_2$ (Ch = S, Se) materials.[37,55] Nonetheless, attempts to fit our data with lower symmetry unit cells (such as $P1$) failed to describe longer range ordering (>10 Å).
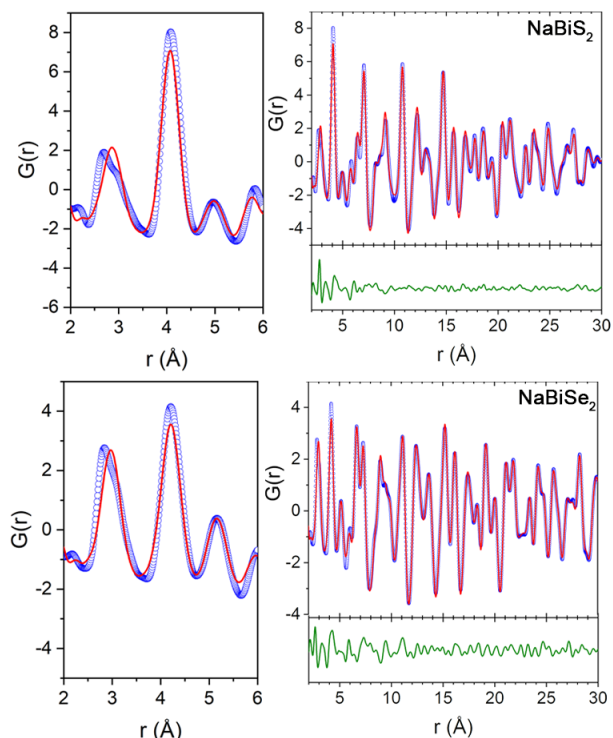

Figure 5. PDF plot of rock salt NaBiS$_2$ and NaBiSe$_2$ nanocrystals. Experimental and $Fm\bar{3}m$ model data are shown in blue and red, respectively. The difference curve of G(r) between the model and the experimental data is shown at the bottom in green. To the right of each plot is the low r region highlighting the asymmetry in the first peak of the data.

From the PDF analysis, we conclude that the lone pair activity of lighter pnictogens has a very large effect on the crystal structure of solution grown I-V-VI$_2$ nanocrystals. In particular, the presence of the pnictogens with more stereoactive lone pairs such as As in LiAsSe$_2$ leads to strong deviations from octahedral coordination.[40] Sb also has strong deviations from octahedral coordination due to lone pair distortions, however Bi has smaller distortions due to a less active lone pair. Like other binary and ternary Bi chalcogenides, suppression of the

stereoactivity of the Bi $6s^2$ electron lone pair due to relativistic effects is observed. Structural analysis thus affirms the need for more in-depth studies beyond standard powder or single crystal X-ray diffraction for these and similar materials.

Crystal Orbital Hamilton Population and Electron Localization Function. Crystal orbital Hamilton population (COHP) was calculated for the Sb-S interactions in three $NaSbS_2$ polymorphs (P_1, C_2/c, and a supercell of $Fm\overline{3}m$) as well as for the Bi-S interactions in $NaBiS_2$ (supercell of $Fm\overline{3}m$). In all cases, the pnictogen-sulfur interaction is not optimized because it contains antibonding contributions below the Fermi level, which are destabilizing. Relaxing the crystal structure from regular SbS_6 octahedra in $Fm\overline{3}m$ to strongly distorted SbS_6 octahedra in C_2/c and P_1 reduces the antibonding Sb-S states (Figure 6 and SI). This supports our PDF findings and provides a rational explanation for why the structure distorts. One remaining question is whether the distortion is caused by optimization of the Sb-S bonding due to its nearest neighbors or by the stereochemical activity of $5s^2$ lone-pair.
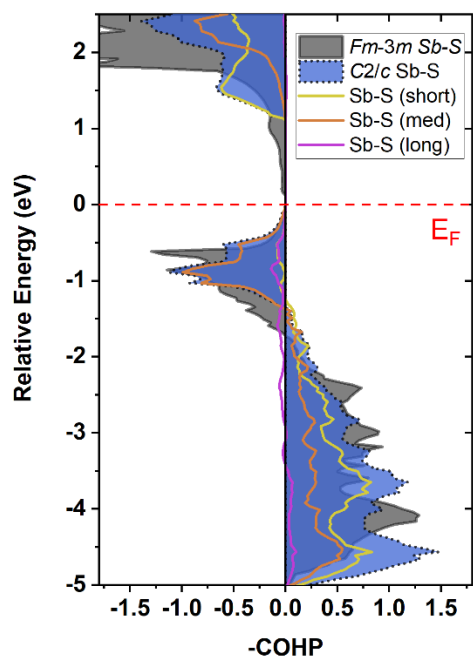

Figure 6. COHP of two polymorphs of $NaSbS_2$. Cubic $NaSbS_2$ (gray) has a higher level of antibonding states than the monoclinic polymorph (blue). The monoclinic structure has 3 different lengths of Sb-S bonds and the respective partial COHP are shown for short Sb-S (yellow), medium Sb-S (orange), and long Sb-S (purple) interactions.

To better understand this, we performed analysis of the chemical bonding in direct space using the electron localization function (ELF). The presence of a Sb electron lone pair pointing toward three distinct S atoms is clearly visible in the C_2/c structure of $NaSbS_2$ (Figure 7), while such electron-pair is absent in the cubic structures of either Sb or Bi analogs. Further, polar covalent bonds are

present at short Sb-S interatomic distances, while longer Sb-S interactions have more ionic character, like the Sb-S interactions in the cubic polymorph. The presence of the stereochemically active Sb $5s^2$ lone pair distorts the octahedron, leading to displacement of the Sb off its center, forming short covalent Sb-S bonds. This in turn, leads to a reduction of the overall antibonding character of the Sb-S interaction. For Bi^{3+}, the stereoactivity of the $6s^2$ electron lone pair is suppressed because of the relativistic effect and lanthanide contraction, which results in more ionic Bi-S interactions inside regular BiS_6 octahedra. Similar trends are seen in the Sn^{2+} and Pb^{2+} containing tungstates and perovskites.[56,57]
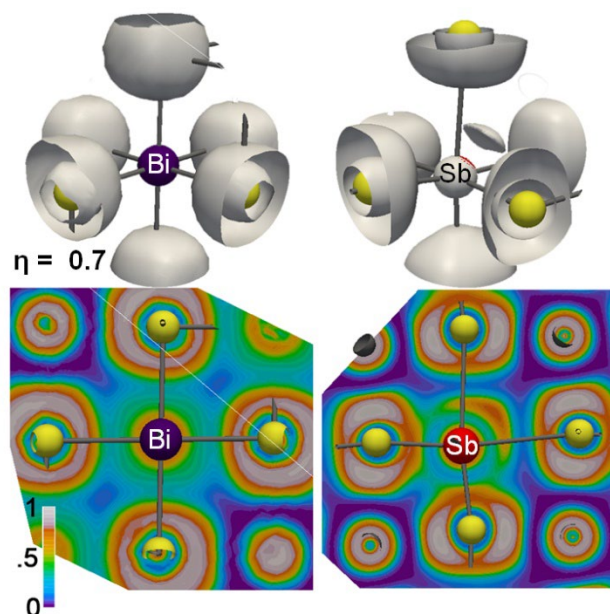

Figure 7. ELF isosurface for $\eta = 0.7$ (top) and 2D slices (bottom) of $NaBiS_2$ ($Fm\overline{3}m$) and $NaSbS_2$ (C_2/c). ELF analysis shows that Sb has a localized lone pair while Bi does not.

Additional Bulk and Surface Characterization. Transmission electron microscopy (TEM) measurements are consistent with the afore-mentioned observations (see SI). For example, elemental analysis of slightly prolate (oval-like) 33±8 nm $NaSbS_2$ nanocrystals by energy dispersive X-ray spectroscopy (EDX) yields a slightly metal–rich stoichiometry of $Na_{0.95}Sb_{1.13}S_2$. Similar small compositional variations are known to occur due to vaporization of light metals under the electron-beam.[58] Alternatively, this slightly-off stoichiometry could be the presence of small amounts of Sb-containing ligands, such as unreacted $SbPh_3$, which may remain bound to the $NaBiS_2$ nanocrystal surface—see solid state NMR measurements below.[21,50,59] Nanocrystals of $NaSbSe_2$ show a cuboidal morphology with a wider diameter distribution of 140±120 nm (SI).

Thermogravimetric analysis (TGA) and differential scanning calorimetry (DSC) provides valuable information about the thermal stability of $APnCh_2$ nanocrystals. $ASbSe_2$ and $NaBiCh_2$ undergo 10–13% mass loss between 300–435 °C, which is likely associated with

the loss of surface ligands (SI).[60] Interestingly, 78–90 % of ASbSe$_2$ ternaries, but only 48–65% of NaBiCh$_2$ ternaries remain as the main crystalline phase, indicating that the Sb-based materials may be more thermally robust than the Bi-based materials; however, this could also be due to the larger particle size of the former (Table 1). Interestingly, the remainder of the crystalline phases after heating is Sb$_2$O$_3$ for ASbSe$_2$, Bi for NaBiS$_2$, and Bi$_2$Se$_3$ for NaBiSe$_2$ (see SI).

The IR spectra of all the as made APnCh$_2$ nanocrystals show vibrational modes consistent with the presence of surface ligands containing hydrocarbon chains, including a ν_s(C-H) stretch at ~2950 cm^{-1} and δ_s(CH$_2$) at ~1450 cm^{-1}. All spectra also show vibrational modes that are characteristic of oleyl amine bound to the nanocrystal surface, including a ν(NH$_2$) stretch at ~3300 cm^{-1}, a (N-H) bending shoulder at ~1600 cm^{-1}, and a ν(C-N) stretch at ~1100 cm^{-1}.[21] In contrast to free oleyl amine, which displays two ν_s(NH$_2$) and ν_{as}(NH$_2$) frequencies by IR, the presence of the single stretch indicates the NH$_2$ headgroup may be hydrogen bonded with nearby ligands—such as S^{2-} or COO$^-$—that may also be present on the nanocrystal surface.[21,61]

In addition to hydrocarbons and amine, the IR spectra of the as made NaSbS$_2$, NaBiS$_2$, and NaBiSe$_2$ nanocrystals—but not LiSbSe$_2$, NaSbSe$_2$, which were prepared in the absence of carboxylates—show two strong bands in the ~1400–1650 cm^{-1} range, which are characteristic of carboxylate vibrational modes.[62] The small difference (Δ) between these two asymmetric (ν_{as}COO$^-$) and symmetric (ν_sCOO$^-$) stretching frequencies confirms that carboxylates (oleate and/or acetate) are bound to the ternary nanocrystal surface in a bidentate (η^2) or chelating fashion. Interestingly, the Δ value for the higher temperature (300 °C), cation ordered $P1$ NaSbS$_2$ phase (104 cm^{-1}) is distinctively larger than that for the lower temperature (200 °C), cation disordered $Fm\overline{3}m$-like NaSbS$_2$ phase (91 cm^{-1}) (SI). In other words, polymorphism and variations in long range ordering in different NaSbS$_2$ samples is substantive enough to impact the exact mode of ligand binding to the nanocrystal surface. In contrast to what is observed for carboxylate binding on the ternary nanocrystals, large Δ values of well over >200 cm^{-1} are observed for monodentate (η^1) binding of carboxylates in precursors such as in oleic acid (254 cm^{-1}) or Sb(OAc)$_3$ (209 cm^{-1}).[62]

We further investigated the surface structures of APnCh$_2$ nanocrystals with ^{1}H solid-state NMR experiments, which provide the highest sensitivity and can differentiate functional groups on the surface ligands (Figure 8). The main observable NMR signals cover a chemical shift range of $ca.$ 0–2.5 ppm and correspond to protons within the long aliphatic alkyl chain of oleylamine and, in some cases, oleate too (see above). The signal that resonates at $ca.$ 5.3 ppm is attributed to the alkenyl protons from oleylamine. Interestingly, the broad signal centered at $ca.$ 7.8 ppm is assigned to phenyl protons from triphenyl antimony or bismuth (Ph$_3$Sb or Ph$_3$Bi). Further, the spectrum of the LiSbSe$_2$ nanocrystals shows two additional broad ^{1}H NMR signals at $ca.$ 3.6 and

below 0 ppm which are assigned to protons that are in close proximity to surface Li sites. The exact assignment are likely surface absorbed water molecules (3.6 ppm) and hydride protons from unreacted LiH (below 0 ppm). To selectively probe spatially closed (dipolar coupled) ^{7}Li and ^{1}H spin pairs in the LiSbSe$_2$ nanocrystals, we performed ^{7}Li spin echo and ^{1}H-detected ^{7}Li → ^{1}H dipolar-refocused insensitive nuclei enhanced by polarization transfer (D-RINEPT) solid-state NMR experiments (Figure 9). The ^{7}Li spin echo NMR spectrum shows signals from all Li species present in the sample, including Li in the bulk of the nanocrystals (the main observable NMR signal at $ca.$ -1 ppm) and proximate to ligands and residual LiH (broad signal at $ca.$ 2.5 ppm). The 2D ^{7}Li → ^{1}H D-RINEPT spectrum shows the ^{7}Li signal at $ca.$ 2.5 ppm, confirming these assignments. The ^{1}H dimension of the 2D ^{7}Li → ^{1}H D-RINEPT spectrum shows signals from the ligands including H$_2$O (δ = 3.6 ppm), CH$_2$ groups within the long aliphatic alkyl chains of oleylamine (δ = 0–2.5 ppm), and LiH (δ < 0 ppm). The enhanced relative intensity of LiH ^{1}H NMR signals in the projection of the D-RINEPT spectrum as compared to the ^{1}H spin echo spectrum is expected because the short internuclear distances and strong dipolar couplings in LiH.
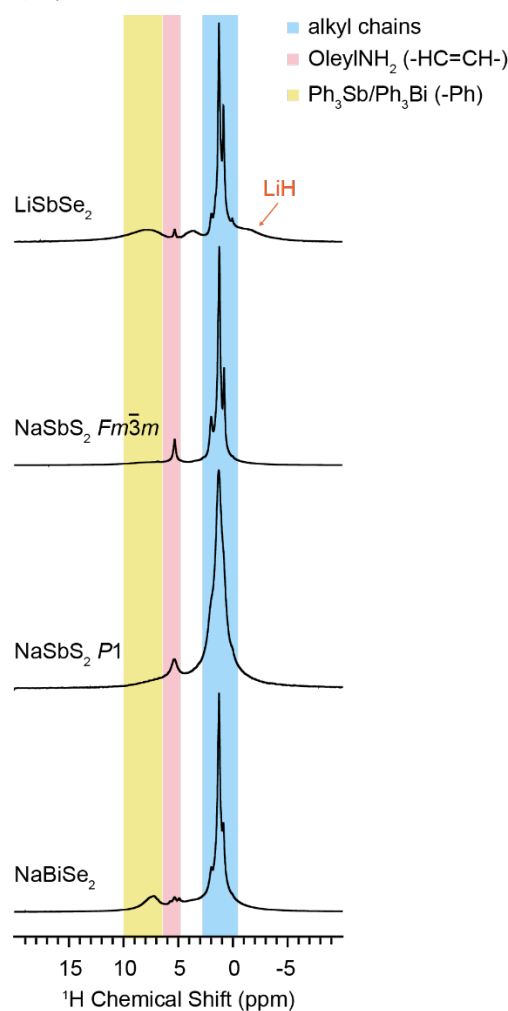

Figure 8. Magic angle spinning (MAS) ^{1}H spin echo solid-state NMR spectra of select APnCh$_2$ nanocrystals.
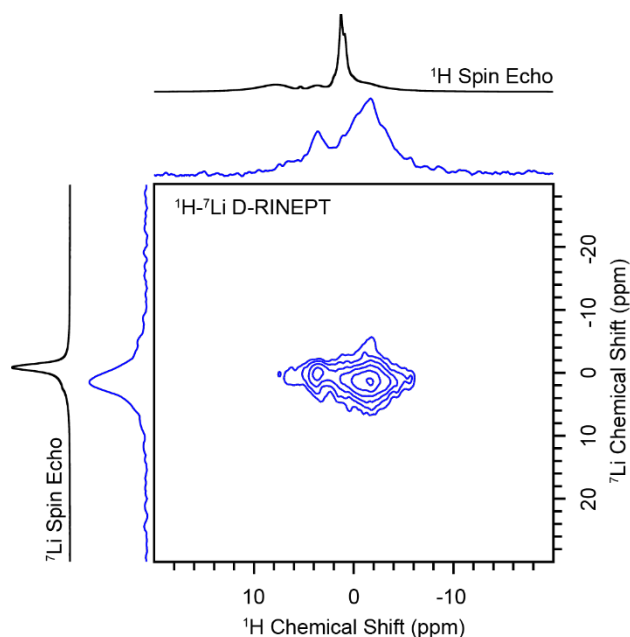
Figure 9. [1]H spin echo, [7]Li spin echo and surface selective [1]H-detected 2D [7]Li → [1]H D-RINEPT of LiSbSe$_2$ nanocrystals.

To probe the composition and structure of the Na sites in Na-containing ternary nanocrystals, we performed ^{23}Na spin echo NMR experiments (SI). The ^{23}Na spin echo NMR spectra show signals from all Na species present in the sample, including Na in the bulk of the nanocrystals and surface Na sites. However, for large nanocrystals with diameters > 50 nm, the majority of atoms are located in the bulk. Therefore, the intense ^{23}Na NMR signal at *ca.* 15.7 ppm is most likely attributed to bulk Na ions. Multiple quantum magic angle spinning (MQMAS) experiments[63,64] were used to resolve overlapping or superimposed resonances (Figure 10). In all cases, the isotropic dimension of the MQMAS spectrum shows broadening, confirming that a distribution of isotropic chemical shifts contributes to the broadening of the Na NMR spectra, in addition to broadening by the second-order quadrupolar interaction. The distribution in isotropic [23]Na chemical shifts is consistent with the disorder of the structures evidenced by powder XRD and PDF analyses. Interestingly, the higher temperature, *P1* NaSbS$_2$ nanocrystals show significantly narrowed ^{23}Na NMR spectra, as compared to the lower synthetic temperature. Narrowing of the ^{23}Na NMR spectra would be expected as a consequence of additional ordering observed in the higher temperature *P1* structure, as indicated from PDF analysis (see above).
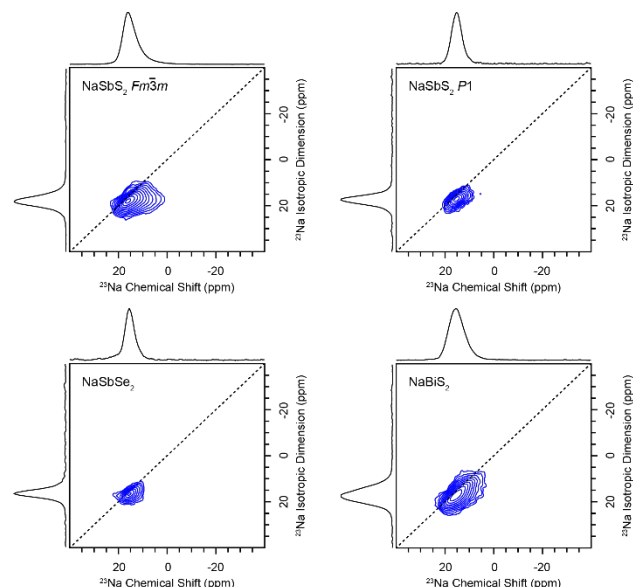

Figure 10. 2D contour plot of [23]Na MQMAS spectra of some NaPnCh$_2$ nanocrystals.

CONCLUSION

In summary, we have successfully prepared several nanocrystalline alkali-based I-V-VI$_2$ semiconductors through a versatile and widely applicable solution-phase soft-chemistry approach. Through synthetic manipulation, we demonstrate control of polymorphism in ternary NaSbS$_2$. These results are confirmed by pair distribution function (PDF) analyses which, in comparison to traditional powder X-ray diffraction, provides insight into the local coordination environments around the Sb and Bi atoms as well as the long-range order.

We also present some of the first PDF analyses of LiSbSe$_2$, NaSbSe$_2$, NaBiS$_2$, and NaBiSe$_2$ materials, which strongly indicate that nanocrystalline forms of the Sb-containing ternaries are significantly distorted due to the stereochemical activity of the Sb $5s^2$ lone pair. Our results confirm expected chemical trends with Sb having more active lone pairs than Bi, as well as the sulfides exhibiting greater distortions than the selenides. Additionally, the PDF analyses show better fits for noncentrosymmetric structural models. The presence of second harmonic oscillator (SHG) activity agrees with the noncentrosymmetric structure of NaSbS$_2$, as obtained from PDF analysis. Further, electron localization function (ELF) analysis enables visualization of the $5s^2$ lone pair, while crystal orbital Hamilton population (COHP) analysis provides insight into the energetic benefits for the adopted, distorted rock salt structure. The stereoactivity of the lone pairs also has implications on the properties. Such lone pair distortions have been shown to reduce thermal conductivity[39] and enhance the dielectric effect in halide perovskites.[65]

Vibrational spectroscopy shows that alkali-based I-V-VI$_2$ nanocrystals are coated with surface-bound oleylamine and, when used, carboxylate ligands. [1]H, ^{7}Li, and ^{23}Na solid state NMR experiments confirm these

results, additionally revealing the presence of small amounts of unreacted LiH (in LiSbSe$_2$) and PnPh$_3$ (in APnSe$_2$) precursor impurities bound to the nanocrystal surfaces. We hope these findings will help move forward further fundamental studies of alkali pnictogen dichalcogenide materials, thus advancing their applications to energy conversion technologies.

METHODS

Materials. Oleylamine (oleylNH$_2$, technical grade, 70%), 1-octadecene (ODE, 90%), sodium hydride (NaH, 99%), and acetone (≥99.5%) were purchased from Sigma-Aldrich; sodium oleate (99%), antimony acetate (97%), triphenyl antimony (97%), tris(dimethylamino)antimony (Sb(NMe$_2$)$_3$, 99.99%) and triphenylbismuth (99%) from Strem; sulfur (99.999%) and lithium hydride (LiH, 97%) from Alfa Aesar; toluene (99.9%), hexanes (99.9%), and methanol (99.9%) from Fisher; silicon powder (Si^0, SRM 640D) from NIST. All chemicals were used as received.

Synthesis. *0.1 M Antimony(III) acetate stock solution.* Antimony(III) acetate (328 mg, 1.1 mmol) was added to oleylamine (10 mL) in a glove box. The solution was stirred and heated to ~100 °C until antimony(III) acetate dissolved. The solution was stored in the glovebox for further use. *0.1 M Se-ODE stock solution.* Se powder (157 mg, 0.002 mol) was added to 20 mL of ODE and degassed at 100°C for 30 min. The mixture was heated to 200°C for 2 h until homogenous. The solution was cooled and stored in a glove box for further use. *Synthesis of NaSbS$_2$.* Sodium oleate (0.11 mmol, 35 mg), S (0.22 mmol, 7.3 mg), and oleylamine (4 mL) were stirred and degassed at room temperature for 10 min. The flask was refilled with Argon (Ar) and antimony acetate stock solution (0.11 mmol Sb, 1 mL) was injected at room temperature. After further degassing at 60 °C for 30 min, the mixture was heated to under Ar to 100–300°C for 30 min. *Synthesis of APnSe$_2$ (A = Li, Na; Pn = Sb, Bi).* NaBiSe$_2$ was prepared as described recently.[50] In a glove box, AH (0.11 mmol), PnPh$_3$ (0.11 mmol), Se-ODE stock solution (2.3 mL), oleylamine (2.7 mL), and a stir bar were added to a round bottom flask. The mixture was transferred to a Schlenk line and degassed at 60 °C for 30 min. The temperature was raised to 290 °C (LiSbSe$_2$) and 300 °C (NaBiSe$_2$) for 1–10 min. *Purification.* The crude solution (~1.0 mL) was diluted with ethanol (5 mL) and centrifuged at 5000 rpm for 5 min. The supernatant was discarded, and the precipitate was solubilized with hexanes (~0.5–1 mL) and sonicated for 1 min. The solids were isolated by diluting with ethanol (5mL) and centrifugation at 5000 rpm for 5 min.

Structural and Compositional Characterization. *Powder X-ray diffraction* patterns were measured using Cu Kα radiation on a Rigaku Ultima IV (40 kV, 44 mA) diffractometer using a background-less quartz sample holder. Scherrer analysis was performed with Match! using a κ value of 0.9. Internal standard of Silicon powder (Si^0, a$_0$=5.43123Å, 640D) was used for line position and Scherrer size. *Transmission Electron Microscopy* imaging was performed on a FEI Tecnai G2-F20 scanning transmission electron microscope. *Pair Distribution*

Function (PDF) Analysis. X-ray total scattering was performed at the Advanced Photon Source, Argonne National Laboratory beamline 11-ID-B. Around 50 mg of sample was loaded into a 0.8 mm diameter Kapton capillary. Data was collected over 3000 0.1 s exposures at room temperature with a detector distance of 180 mm. The X-ray wavelength was 0.2115 Å. To obtain the scattering structure factor S(Q), corrections for background and container scattering, X-ray transmission, and Compton scattering were applied using PDFgetX3.[66] S(Q) was truncated at a Q$_{max}$ value ranging from 21 to 23 Å^{-1} and the PDF was calculated. All fitting of the PDF data was carried out in PDFgui.[67] For each refinement, *Qdamp* and *Qbroad* were kept constant at 0.04 Å^{-1} and 0.01 Å^{-1}, respectively. Initial refinements were carried out with a cutoff of 10 Å. Subsequently, the unit cell parameters were refined, followed by the atomic positions of Sb/Bi, S/Se, and then Na. The position of Li was not able to be refined reliably so its position was kept fixed. Each parameter was refined independently to avoid correlation between parameters in the initial steps. Once the unit cell and atomic positions were refined the anisotropic displacement parameters (ADPs) of each atom type were refined independently (excluding Li, Na where isotropic displacement was used). The last parameter to be refined was "delta 1" which is the linear atomic correlation factor that arises from correlated atomic motion. The refinement of delta 1 improved the fit of the nearest neighbor peak significantly as expected. A final round of refinement included the gradual introduction of more and more parameters until all parameters were refined together. The results of the refinements are summarized in in the Supporting Information (SI) file.

Spectroscopic Characterization. *Diffuse-reflectance* spectra were measured with a SL1 Tungsten Halogen lamp (vis-IR), a SL3 Deuterium lamp (UV), and a BLACK-Comet C-SR-100 spectrometer. Samples were prepared by drop-casting hexane solutions onto glass slides. *Band gap values* were estimated by extrapolating the linear slope of Tauc plots by plotting (Ahν)$^{1/r}$ *vs.* hν where A = absorbance, hν = incident photon energy in eV, r = ½ for direct and r = 2 for indirect semiconductors. *Infrared (IR) spectroscopy* measurements were performed on a Bruker Tensor 37 Fourier transform IR spectrophotometer (64 scans, transmittance mode, 4 cm^{-1} resolution). *Transient absorption* experiments were performed using a commercial, amplified Ti:sapphire laser operating at 2 kHz, 800 nm, and 35 fs pulsewidth. A portion of the output was time-delayed and focused into either sapphire or yttrium aluminum garnet to produce white light probe pulses in the visible or near-infrared, respectively. The pump pulses were reduced in repetition rate to 1 kHz and overlapped with the probe pulse to produce transient absorption signals by comparing transmitted probe beam with pump on vs pump off. *Raman spectroscopy* analysis was performed on an XploRA Plus confocal Raman microscope (HORIBA Scientific, Edison, NJ) using a 785-nm excitation laser at 0.4 mW and a 50× (0.5 NA) long working distance

objective. All measurements were taken with a diffraction grating of 600 gr/mm with an acquisition time of 60 s. Six locations throughout each sample—2 accumulations averaged per location—were collected.

NMR Spectroscopy Methods. All moderate field [B_o = 9.4 T, $\nu_o(^1H)$ = 400 MHz, $\nu_o(^7Li)$ = 155.5 MHz, $\nu_o(^{23}Na)$ = 105.8 MHz, and $n_o(^{77}Se)$ = 76.3 MHz] solid-state NMR (SSNMR) experiments were performed on a Bruker Avance III HD spectrometer with a wide-bore magnet. A Bruker 2.5 mm HXY triple-resonance MAS probe was used to perform all MAS experiments at a spinning rate (ν_{rot}) of 25 kHz. ^1H NMR shifts were referenced to neat tetramethylsilane using adamantane [$\delta_{iso}(^1H)$ = 1.82 ppm] as a secondary standard. Previously published relative NMR frequencies were used to indirectly reference ^7Li, ^{23}Na, and ^{77}Se chemical shifts.[68] All experiments were performed using optimum recycle delays of $1.3 \times T_1$. All the NMR spectra were processed in Topspin 3.6. *^1H SSNMR.* ^1H MAS NMR spectra were acquired using a spin echo sequence with $\pi/2$ and π pulses of 2.5 and 5 μs, respectively. ^1H radiofrequency (RF) fields were calibrated directly on each sample. *^7Li SSNMR.* ^7Li MAS NMR spectra were acquired using a spin echo sequence with central transition (CT) selective $\pi/2$ and π pulse lengths of 2.5 and 5 μs, respectively. ^1H-detected $^7Li \rightarrow ^1H$ dipolar refocused insensitive nuclei enhanced by polarization transfer (D-RINEPT) spectra were obtained with symmetry based recoupling sequence super-cycled (S) $R4^2_1$ to the ^1H nuclei during the INEPT evolution times to recouple heteronuclear dipolar couplings.[69–71] The rf field for $SR4^2_1$ recoupling was set to two times the sample spinning rate to fulfill the second order rotary resonance recoupling (R_3) condition.[69,72] A relative short recoupling time of two rotor cycles (80 μs) per recoupling block was applied for near-surface characterization. The total recoupling time ($4 \times 2 \times \tau_r$) was 0.32 ms. *^{23}Na SSNMR.* ^{23}Na MAS NMR spectra were acquired using a spin echo sequence with central transition (CT) selective $\pi/2$ and π pulse lengths of 4.7 and 9.4 μs, respectively. The RAPT pulses are incorporated into ^{23}Na spin echo and population transfer (PT) $^{23}Na\{^{77}Se\}$ D-HMQC pulse sequence providing further improvements in sensitivity by a factor ~ 1.7.[73–75] WURST pulses 38.0 μs in duration (followed by 2 μs of delay) with an rf field of 100 kHz were applied repeatedly in the RAPT blocks used in PT D-HMQC experiments. The frequency sweep width of the RAPT pulses was equal to the MAS frequency in all cases. The frequency offset of the WURST pulses was alternated between ± 325 kHz. The rotational echo double resonance (REDOR) was applied to the ^{77}Se nuclei in order to recouple heteronuclear dipolar couplings.[76,77] The number of rotor cycles for each REDOR dipolar recoupling block was optimized to 100. The total recoupling time ($2 \times 100 \times \tau_r$) was 8000 μs. Multiple quantum magic angle spinning (MQMAS) NMR spectra were obtained with a split-t_1, z-filtered pulse sequence.[63,64] The indirect dimension frequency axis was divided by a factor 2.125 to account for the scaled evolution of the isotropic chemical shifts.[78] The length of the 3Q-excitation and the reconversion pulses were obtained by optimizing them on each sample directly. Typically, high-power 3Q-excitation and reconversion pulse widths were ca. 3.6 μs and 1.3 μs, respectively, with an ^{23}Na rf field of ca. 115.5 kHz (ca. 231 kHz CT nutation frequency). *^{77}Se SSNMR.* ^{77}Se MAS NMR spectra were acquired using a spin echo sequence with $\pi/2$ and π pulse lengths of 2.8 and 5.6 μs, respectively.

Second Harmonic Generation. Based on the Kurtz and Perry method, powder SHG response was investigated by a *Q*-switch pulse laser (2.09 μm, 3 Hz, 50 ns) with four different particle sizes, presumably of agglomerates of nanocrystallites, including 38-55, 55-88, 88-105 and 200-250 μm. In view of its relatively narrow bandgap, the SHG response may be seriously weakened with the direct-transmittance measurement. Thus, in this work, we chose the more efficient measurement by collecting the special reflectance SHG intensity signals on the sample surface instead of common transmittance signals, and this method was confirmed elsewhere.[79]

Calculations. Total energy calculations were performed using the Vienna Ab-initio Simulation Package (VASP).[80] The projected augmented-wave (PAW) pseudopotentials with the local density approximation (LDA) were used with a cutoff energy of 500 eV and a convergence energy of 1×10^{-4} eV. The tetrahedron method and Blöchl corrections were used with a dense k-point mesh when calculating total energy. The 2x2x2 cubic supercells used a k-point mesh of 10x10x10. NaSbS$_2$ in $P\overline{1}$ symmetry used a 20x20x16 k-point mesh. NaSbS$_2$ in $C2/c$ symmetry used a k-point mesh 14x14x16. NaSbS$_2$ in $C2/m$ symmetry used a k-point mesh of 8x20x20 k-point mesh. Unit cell volume, cell shape, and atomic positions were relaxed sequentially, then simultaneously. COHP[81] and ELF[82–84] were calculated using the linear muffin tin orbital atomic sphere approximation (LMTO-ASA) code version 47c.[85] Mixing of the Na/Sb sites in the $Fm\overline{3}m$ structure of NaSbS$_2$ was handled by using a supercell referred to as 33mer. The $C2/c$ model used the optimized structure from Sun et al.,[29] while the P1 model was taken from the results of PDF refinement. The COHP and ELF of NaBiS$_2$ were calculated using the lowest energy coloring structure referred to as 33facL1.[50]

ASSOCIATED CONTENT

Supporting Information

Additional DFT calculations, powder XRD, thermal analyses (TGA/DSC), IR spectra, TEM images, diffuse reflectance, PDF analysis and data, and NMR spectra. This Supporting Information is available free of charge on the ACS Publications website.

AUTHOR INFORMATION

Corresponding Author

* vela@iastate.edu
* kovnir@iastate.edu

‡Equal contribution authors

Authors:

Alan Medina-Gonzalez– Department of Chemistry, Iowa State University, Ames, Iowa, 50011, United States.

Philip Yox – Department of Chemistry, Iowa State University, Ames, Iowa, 50011, United States; Ames Laboratory, U.S. Department of Energy, Ames, Iowa, 50011, United States.

Yunhua Chen – Department of Chemistry, Iowa State University, Ames, Iowa, 50011, United States; Ames Laboratory, U.S. Department of Energy, Ames, Iowa, 50011, United States.

Marquix A. S. Adamson – Department of Chemistry, Iowa State University, Ames, Iowa, 50011, United States.

Bryan A. Rosales– Department of Chemistry, Iowa State University, Ames, Iowa, 50011, United States.

Maranny Svay – Department of Chemistry, Iowa State University, Ames, Iowa, 50011, United States.

Emily A. Smith – Department of Chemistry, Iowa State University, Ames, Iowa, 50011, United States; Ames Laboratory, U.S. Department of Energy, Ames, Iowa, 50011, United States.

Richard D. Schaller – Department of Chemistry, Northwestern University, Evanston, Illinois, 60208, United States; Center for Nanoscale Materials, US DOE Argonne National Laboratory, Lemont, Illinois, 60439, United States.

Kui Wu – College of Chemistry and Environmental Science, Hebei University, Baoding City, Hebei Province, 071002, China.

Aaron J. Rossini – Department of Chemistry, Iowa State University, Ames, Iowa, 50011, United States; Ames Laboratory, U.S. Department of Energy, Ames, Iowa, 50011, United States.

Kirill Kovnir – Department of Chemistry, Iowa State University, Ames, Iowa, 50011, United States; Ames Laboratory, U.S. Department of Energy, Ames, Iowa, 50011, United States.

Javier Vela – Department of Chemistry, Iowa State University, Ames, Iowa, 50011, United States; Ames Laboratory, U.S. Department of Energy, Ames, Iowa, 50011, United States.

ACKNOWLEDGMENT

REFERENCES

(1)   Pei, Y.; LaLonde, A.; Iwanaga, S.; Jeffrey Snyder, G. High Thermoelectric Figure of Merit in Heavy Hole Dominated PbTe. *Energy Environ. Sci.* **2011**, *4* (6), 2085–2089. DOI: 10.1039/C0EE00456A.

(2)   Kanatzidis, M. G. Nanostructured Thermoelectrics: The New Paradigm? †. *Chem Mater* **2010**, *22*, 648–659. DOI: 10.1021/cm902195j.

(3)   Delaire, O.; Ma, J.; Marty, K.; May, A. F.; McGuire, M. A.; Du, M.-H.; Singh, D. J.; Podlesnyak, A.; Ehlers, G.; Lumsden, M. D.; Sales, B. C. Giant Anharmonic Phonon Scattering in PbTe. *Nat. Mater.* **2011**, *10* (8), 614–619. DOI: 10.1038/nmat3035.

(4)   Lee, S.; Esfarjani, K.; Luo, T.; Zhou, J.; Tian, Z.; Chen, G. Resonant Bonding Leads to Low Lattice Thermal Conductivity. *Nat. Commun.* **2014**, *5* (1), 3525. DOI: 10.1038/ncomms4525.

(5)   Slade, T. J.; Pal, K.; Grovogui, J. A.; Bailey, T. P.; Male, J.; Khoury, J. F.; Zhou, X.; Chung, D. Y.; Snyder, G. J.; Uher, C.; Dravid, V. P.; Wolverton, C.; Kanatzidis, M. G. Contrasting SnTe–NaSbTe$_2$ and SnTe–NaBiTe$_2$ Thermoelectric Alloys: High Performance Facilitated by Increased Cation Vacancies and Lattice Softening. *J. Am. Chem. Soc.* **2020**, *142* (28), 12524–12535. DOI: 10.1021/jacs.0c05650.

(6)   Slade, T. J.; Grovogui, J. A.; Hao, S.; Bailey, T. P.; Ma, R.; Hua, X.; Guéguen, A.; Uher, C.; Wolverton, C.; Dravid, V. P.; Kanatzidis, M. G. Absence of Nanostructuring in NaPb$_m$SbTe$_{m+2}$: Solid Solutions with High Thermoelectric Performance in the Intermediate Temperature Regime. *J. Am. Chem. Soc.* **2018**, *140* (22), 7021–7031. DOI: 10.1021/jacs.8b04193.

(7)   Li, N.; He, W.; Li, C.; Wang, G.; Wang, G.; Zhou, X.; Lu, X. The Role of Electronegativity in the Thermoelectric Performance of GeTe–I–V–VI$_2$ Solid Solutions. *J. Mater. Chem. A* **2021**, *9* (4), 2385–2393. DOI: 10.1039/D0TA10268G.

(8)   Hsu, K. F.; Loo, S.; Guo, F.; Chen, W.; Dyck, J. S.; Uher, C.; Hogan, T.; Polychroniadis, E. K.; Kanatzidis, M. G. Cubic AgPb$_m$SbTe$_{2+m}$: Bulk Thermoelectric Materials with High Figure of Merit. *Science* **2004**, *303* (5659), 818–821. DOI: 10.1126/science.1092963.

(9)   Han, M.-K.; Androulakis, J.; Kim, S.-J.; Kanatzidis, M. G. Lead-Free Thermoelectrics: High Figure of Merit in p-Type AgSn$_m$SbTe$_{m+2}$. *Adv. Energy Mater.*

2012, *2* (1), 157–161. DOI: 10.1002/aenm.201100613.

(10) Du, B.; Li, H.; Xu, J.; Tang, X.; Uher, C. Enhanced Figure-of-Merit in Se-Doped p-Type $AgSbTe_2$ Thermoelectric Compound. *Chem. Mater.* **2010**, *22* (19), 5521–5527. DOI: 10.1021/cm101503y.

(11) Xu, J.; Li, H.; Du, B.; Tang, X.; Zhang, Q.; Uher, C. High Thermoelectric Figure of Merit and Nanostructuring in Bulk $AgSbTe_2$. *J. Mater. Chem.* **2010**, *20* (29), 6138–6143. DOI: 10.1039/C0JM00138D.

(12) Liu, Z.; Shuai, J.; Geng, H.; Mao, J.; Feng, Y.; Zhao, X.; Meng, X.; He, R.; Cai, W.; Sui, J. Contrasting the Role of Mg and Ba Doping on the Microstructure and Thermoelectric Properties of P-Type $AgSbSe_2$. *ACS Appl. Mater. Interfaces* **2015**, *7* (41), 23047–23055. DOI: 10.1021/acsami.5b06492.

(13) Samanta, M.; Roychowdhury, S.; Ghatak, J.; Perumal, S.; Biswas, K. Ultrahigh Average Thermoelectric Figure of Merit, Low Lattice Thermal Conductivity and Enhanced Microhardness in Nanostructured $(GeTe)_x(AgSbSe_2)_2$-x. *Chem. Euro. J.* **2017**, *23*, 1–7.

(14) N. Guin, S.; S. Negi, D.; Datta, R.; Biswas, K. Nanostructuring, Carrier Engineering and Bond Anharmonicity Synergistically Boost the Thermoelectric Performance of p-Type $AgSbSe_2$–ZnSe. *J. Mater. Chem. A* **2014**, *2* (12), 4324–4331. DOI: 10.1039/C3TA14901C.

(15) Cai, S.; Liu, Z.; Sun, J.; Li, R.; Fei, W.; Sui, J. Enhancement of Thermoelectric Properties by Na Doping in Te-Free p-Type $AgSbSe_2$. *Dalton Trans.* **2014**, *44* (3), 1046–1051. DOI: 10.1039/C4DT03059A.

(16) Poudeu, P. F. P.; D'Angelo, J.; Downey, A. D.; Short, J. L.; Hogan, T. P.; Kanatzidis, M. G. High Thermoelectric Figure of Merit and Nanostructuring in Bulk P-Type $Na_{1-x}Pb_mSb_yTe_{m+2}$. *Angew. Chem. Int. Ed.* **2006**, *45* (23), 3835–3839. DOI: 10.1002/anie.200600865.

(17) Morelli, D. T.; Jovovic, V.; Heremans, J. P. Intrinsically Minimal Thermal Conductivity in Cubic I-V-VI_2 Semiconductors. *Phys. Rev. Lett.* **2008**, *101* (3), 035901. DOI: 10.1103/PhysRevLett.101.035901.

(18) D. Nielsen, M.; Ozolins, V.; P. Heremans, J. Lone Pair Electrons Minimize Lattice Thermal Conductivity. *Energy Environ. Sci.* **2013**, *6* (2), 570–578. DOI: 10.1039/C2EE23391F.

(19) Roychowdhury, S.; Ghosh, T.; Arora, R.; Samanta, M.; Xie, L.; Singh, N. K.; Soni, A.; He, J.; Waghmare, U. V.; Biswas, K. Enhanced Atomic Ordering Leads to High Thermoelectric Performance in $AgSbTe_2$. *Science* **2021**, *371* (6530), 722–727. DOI: 10.1126/science.abb3517.

(20) Hua, X.; I. Hegde, V.; Wolverton, C. Phase Stability and Ordering in Rock Salt-Based Thermoelectrics: $NaSbX_2$, $AgSbX_2$, and Their Alloys with PbX and SnX (X = S, Se, Te). *Chem. Mater.* **2019**, *31* (22), 9445–9452. DOI: 10.1021/acs.chemmater.9b03318.

(21) Medina-Gonzalez, A. M.; Rosales, B. A.; Hamdeh, U. H.; Panthani, M. G.; Vela, J. Surface Chemistry of Ternary Nanocrystals: Engineering the Deposition of Conductive $NaBiS_2$ Films. *Chem. Mater.* **2020**, *32* (14), 6085–6096. DOI: 10.1021/acs.chemmater.0c01689.

(22) Burgués-Ceballos, I.; Wang, Y.; Akgul, M. Z.; Konstantatos, G. Colloidal $AgBiS_2$ Nanocrystals with Reduced Recombination Yield 6.4% Power Conversion Efficiency in Solution-Processed Solar Cells. *Nano Energy* **2020**, *75*, 104961. DOI: 10.1016/j.nanoen.2020.104961.

(23) Fabini, D. H.; Koerner, M.; Seshadri, R. Candidate Inorganic Photovoltaic Materials from Electronic Structure-Based Optical Absorption and Charge Transport Proxies. *Chem. Mater.* **2019**, *31* (5), 1561–1574. DOI: 10.1021/acs.chemmater.8b04542.

(24) Öberg, V. A.; Johansson, M. B.; Zhang, X.; Johansson, E. M. J. Cubic $AgBiS_2$ Colloidal Nanocrystals for Solar Cells. *ACS Appl. Nano Mater.* **2020**, *3* (5), 4014–4024. DOI: 10.1021/acsanm.9b02443.

(25) Khare, I. S.; Szymanski, N. J.; Gall, D.; Irving, R. E. Electronic, Optical, and Thermoelectric Properties of Sodium Pnictogen Chalcogenides: A First Principles Study. *Comput. Mater. Sci.* **2020**, *183*, 109818. DOI: 10.1016/j.commatsci.2020.109818.

(26) Xia, Z.; Yu, F.-X.; Lu, S.-C.; Xue, D.-J.; He, Y.-S.; Yang, B.; Wang, C.; Ding, R.-Q.; Zhong, J.; Tang, J. Synthesis and Characterization of $NaSbS_2$ Thin Film for Potential Photodetector and Photovoltaic Application. *Chin. Chem. Lett.* **2017**, *28* (4), 881–887. DOI: 10.1016/j.cclet.2017.03.003.

(27) Leung, W. W.; Savory, C. N.; Palgrave, R. G.; Scanlon, D. O. An Experimental and Theoretical Study into $NaSbS_2$ as an Emerging Solar Absorber. *J. Mater. Chem. C* **2019**, *7* (7), 2059–2067. DOI: 10.1039/c8tc06284f.

(28) Liu, D.; Huang, S.; Wang, X.; Sa, R. (Li,Na)SbS_2 as a Promising Solar Absorber Material: A Theoretical Investigation. *Spectrochim. Acta. A. Mol. Biomol. Spectrosc.* **2021**, *250*, 119389. DOI: 10.1016/j.saa.2020.119389.

(29) Sun, J.; Singh, D. J. Electronic Properties, Screening, and Efficient Carrier Transport in $NaSbS_2$. *Phys. Rev. Appl.* **2017**, *7* (2), 024015. DOI: 10.1103/PhysRevApplied.7.024015.

(30) Bazakutsa, V. A.; Gnidash, N. I.; Kul'chitskaya, A. K.; Salov, A. V. Photoelectric and Optical Properties of Thin Films of Ternary Chalcogenides of the Form $Me^ISbX_2^{VI}$. *Sov. Phys. J.* **1975**, *18* (4), 472–475. DOI: 10.1007/BF01093235.

(31) Rahayu, S. U.; Chou, C.-L.; Suriyawong, N.; Aragaw, B. A.; Shi, J.-B.; Lee, M.-W. Sodium Antimony Sulfide ($NaSbS_2$): Turning an Unexpected Impurity into a Promising, Environmentally Friendly Novel Solar Absorber Material. *APL Mater.* **2016**, *4* (11), 116103. DOI: 10.1063/1.4967206.

(32) Kang, Y.; Youn, Y.; Han, S.; Park, J.; Oh, C.-S. Computational Screening of Indirect-Gap Semiconductors for Potential Photovoltaic Absorbers. *Chem. Mater.* **2019**, *31* (11), 4072–4080. DOI: 10.1021/acs.chemmater.9b00708.

(33) Sun, W.-C.; Rahayu, S. U.; Lee, M.-W. Eco-Friendly $NaSbS_2$ Quantum Dot-Sensitized Solar Cells. *IEEE J. Photovolt.* **2018**, *8* (4), 1011–1016. DOI: 10.1109/JPHOTOV.2018.2826044.

(34) Zhang, X.; Huang, M.; Xu, P.; Dai, C.-M.; Cai, Z.-H.; Han, D.; Chen, S. Earth-Abundant Photovoltaic Semiconductor $NaSbS_2$ in the Rocksalt-Derived Structure: A First-Principles Study. *Prog. Nat. Sci. Mater. Int.* **2019**, *29* (3), 322–328. DOI: 10.1016/j.pnsc.2019.02.009.

(35) Mahmoud, M. M. A.; Joubert, D. P.; Molepo, M. P. Structural, Stability and Thermoelectric Properties for the Monoclinic Phase of $NaSbS_2$ and $NaSbSe_2$: A Theoretical Investigation. *Eur. Phys. J. B* **2019**, *92* (9), 214. DOI: 10.1140/epjb/e2019-90712-y.

(36) Harikesh, P. C.; Surendran, A.; Ghosh, B.; John, R. A.; Moorthy, A.; Yantara, N.; Salim, T.; Thirumal, K.; Leong, W. L.; Mhaisalkar, S.; Mathews, N. Cubic $NaSbS_2$ as an Ionic–Electronic Coupled Semiconductor for Switchable Photovoltaic and Neuromorphic Device Applications. *Adv. Mater.* **2020**, *32* (7), 1906976. DOI: 10.1002/adma.201906976.

(37) Rathore, E.; Juneja, R.; Culver, S. P.; Minafra, N.; Singh, A. K.; Zeier, W. G.; Biswas, K. Origin of Ultralow Thermal Conductivity in N-Type Cubic Bulk $AgBiS_2$: Soft Ag Vibrations and Local Structural Distortion Induced by the Bi $6s^2$ Lone Pair. *Chem. Mater.* **2019**, *31* (6), 2106–2113. DOI: 10.1021/acs.chemmater.9b00001.

(38) Bernges, T.; Peilstöcker, J.; Dutta, M.; Ohno, S.; Culver, S. P.; Biswas, K.; Zeier, W. G. Local Structure and Influence of Sb Substitution on the Structure–Transport Properties in $AgBiSe_2$. *Inorg. Chem.* **2019**, *58* (14), 9236–9245. DOI: 10.1021/acs.inorgchem.9b00874.

(39) Dutta, M.; Prasad, M. V. D.; Pandey, J.; Soni, A.; Waghmare, U. V.; Biswas, K. Local Symmetry Breaking Suppresses Thermal Conductivity in Crystalline Solids. *Angew. Chem. Int. Ed.* **2022**, *61* (15), e202200071. DOI: 10.1002/anie.202200071.

(40) Bera, T. K.; Jang, J. I.; Song, J.-H.; Malliakas, C. D.; Freeman, A. J.; Ketterson, J. B.; Kanatzidis, M. G. Soluble Semiconductors $AAsSe_2$ (A = Li, Na) with a Direct-Band-Gap and Strong Second Harmonic Generation: A Combined Experimental and Theoretical Study. *J. Am. Chem. Soc.* **2010**, *132* (10), 3484–3495. DOI: 10.1021/ja9094846.

(41) Iyer, A. K.; Cho, J. B.; Byun, H. R.; Waters, M. J.; Hao, S.; Oxley, B. M.; Gopalan, V.; Wolverton, C.; Rondinelli, J. M.; Jang, J. I.; Kanatzidis, M. G. Structure Tuning, Strong Second Harmonic Generation Response, and High Optical Stability of the Polar Semiconductors $Na_{1-x}K_xAsQ_2$. *J. Am. Chem. Soc.* **2021**, *143* (43), 18204–18215. DOI: 10.1021/jacs.1c07993.

(42) Gvozdetskyi, V.; Lee, S. J.; Owens-Baird, B.; Dolyniuk, J.-A.; Cox, T.; Wang, R.; Lin, Z.; Ho, K.-M.; Zaikina, J. V. Ternary Zinc Antimonides Unlocked Using Hydride Synthesis. *Inorg. Chem.* **2021**, *60* (14), 10686–10697. DOI: 10.1021/acs.inorgchem.1c01381.

(43) Gvozdetskyi, V.; Owens-Baird, B.; Hong, S.; Cox, T.; Bhaskar, G.; Harmer, C.; Sun, Y.; Zhang, F.; Wang, C.-Z.; Ho, K.-M.; Zaikina, J. V. From $NaZn_4Sb_3$ to $HT-Na_{1-x}Zn_{4-y}Sb_3$: Panoramic Hydride Synthesis, Structural Diversity, and Thermoelectric Properties. *Chem. Mater.* **2019**, *31* (21), 8695–8707. DOI: 10.1021/acs.chemmater.9b02239.

(44) Cox, T.; Gvozdetskyi, V.; Owens-Baird, B.; Zaikina, J. V. Rapid Phase Screening via Hydride Route: A Discovery of $K_{8-x}Zn_{18+3x}Sb_{16}$. *Chem. Mater.* **2018**, *30* (23), 8707–8715. DOI: 10.1021/acs.chemmater.8b04211.

(45) Cox, T.; Gvozdetskyi, V.; Bertolami, M.; Lee, S.; Shipley, K.; Lebedev, O. I.; Zaikina, J. V. Clathrate XI $K_{58}Zn_{122}Sb_{207}$: A New Branch on the Clathrate Family Tree. *Angew. Chem.* **2021**, *133* (1), 419–427. DOI: 10.1002/ange.202011120.

(46) Zaikina, J. V.; Batuk, M.; Abakumov, A. M.; Navrotsky, A.; Kauzlarich, S. M. Facile Synthesis of $Ba_{1-x}K_xFe_2As_2$ Superconductors via Hydride Route. *J. Am. Chem. Soc.* **2014**, *136* (48), 16932–16939. DOI: 10.1021/ja509907r.

(47) White, M. A.; J. Thompson, M.; J. Miller, G.; Vela, J. Got LiZnP? Solution Phase Synthesis of Filled Tetrahedral Semiconductors in the Nanoregime. *Chem. Commun.* **2016**, *52* (17), 3497–3499. DOI: 10.1039/C5CC09635A.

(48) White, M. A.; Baumler, K. J.; Chen, Y.; Venkatesh, A.; Medina-Gonzalez, A. M.; Rossini, A. J.; Zaikina, J. V.; Chan, E. M.; Vela, J. Expanding the I–II–V Phase Space: Soft Synthesis of Polytypic Ternary and Binary Zinc Antimonides. *Chem. Mater.* **2018**, *30* (17), 6173–6182. DOI: 10.1021/acs.chemmater.8b02910.

(49) Medina-Gonzalez, A. M.; Yox, P.; Chen, Y.; Adamson, M. A. S.; Svay, M.; Smith, E. A.; Schaller, R. D.; Rossini, A. J.; Vela, J. Ternary ACd_4P_3 (A = Na, K) Nanostructures via a Hydride Solution-Phase Route. *ACS Mater. Au* **2021**, *1* (2), 130–139. DOI: 10.1021/acsmaterialsau.1c00018.

(50) Rosales, B. A.; White, M. A.; Vela, J. Solution-Grown Sodium Bismuth Dichalcogenides: Toward Earth-Abundant, Biocompatible Semiconductors. *J. Am. Chem. Soc.* **2018**, *140* (10), 3736–3742. DOI: 10.1021/jacs.7b12873.

(51) Rodrigues, T. S.; Zhao, M.; Yang, T.-H.; Gilroy, K. D.; da Silva, A. G. M.; Camargo, P. H. C.; Xia, Y. Synthesis of Colloidal Metal Nanocrystals: A Comprehensive Review on the Reductants. *Chem. – Eur. J.* **2018**, *24* (64), 16944–16963. DOI: 10.1002/chem.201802194.

(52) He, M.; Protesescu, L.; Caputo, R.; Krumeich, F.; Kovalenko, M. V. A General Synthesis Strategy for Monodisperse Metallic and Metalloid Nanoparticles (In, Ga, Bi, Sb, Zn, Cu, Sn, and Their Alloys) via in Situ Formed Metal Long-Chain Amides. *Chem. Mater.* **2015**, *27* (2), 635–647. DOI: 10.1021/cm5045144.

(53) Billinge, S. J. L. The Rise of the X-Ray Atomic Pair Distribution Function Method: A Series of Fortunate Events. *Philos. Trans. R. Soc. Math. Phys. Eng. Sci.* **2019**, *377* (2147), 20180413. DOI: 10.1098/rsta.2018.0413.

(54) Tideswell, N. W.; Kruse, F. H.; McCullough, J. D. The Crystal Structure of Antimony Selenide, Sb_2Se_3. *Acta Crystallogr.* **1957**, *10* (2), 99–102. DOI: 10.1107/S0365110X57000298.

(55) Mohn, C. E.; Stølen, S. Influence of the Stereochemically Active Bismuth Lone Pair

Structure on Ferroelectricity and Photocalytic Activity of Aurivillius Phase Bi${}_{2}$$${\mathit{WO}}_{6}$. *Phys. Rev. B* **2011**, *83* (1), 014103. DOI: 10.1103/PhysRevB.83.014103.

(56) Stoltzfus, M. W.; Woodward, P. M.; Seshadri, R.; Klepeis, J.-H.; Bursten, B. Structure and Bonding in SnWO$_4$, PbWO$_4$, and BiVO$_4$: Lone Pairs vs Inert Pairs. *Inorg. Chem.* **2007**, *46* (10), 3839–3850. DOI: 10.1021/ic061157g.

(57) Laurita, G.; Seshadri, R. Chemistry, Structure, and Function of Lone Pairs in Extended Solids. *Acc. Chem. Res.* **2022**, *55* (7), 1004–1014. DOI: 10.1021/acs.accounts.1c00741.

(58) Methods of Surface Characterization https://www.springer.com/series/6309 (accessed 2021 -12 -20).

(59) Anderson, N. C.; Hendricks, M. P.; Choi, J. J.; Owen, J. S. Ligand Exchange and the Stoichiometry of Metal Chalcogenide Nanocrystals: Spectroscopic Observation of Facile Metal-Carboxylate Displacement and Binding. *J. Am. Chem. Soc.* **2013**, *135* (49), 18536–18548. DOI: 10.1021/ja4086758.

(60) Reichert, M. D.; Lin, C.-C.; Vela, J. How Robust Are Semiconductor Nanorods? Investigating the Stability and Chemical Decomposition Pathways of Photoactive Nanocrystals. *Chem. Mater.* **2014**, *26* (13), 3900–3908. DOI: 10.1021/cm500896n.

(61) Cooper, J. K.; Franco, A. M.; Gul, S.; Corrado, C.; Zhang, J. Z. Characterization of Primary Amine Capped CdSe, ZnSe, and ZnS Quantum Dots by FT-IR: Determination of Surface Bonding Interaction and Identification of Selective Desorption. *Langmuir* **2011**, *27* (13), 8486–8493. DOI: 10.1021/la201273x.

(62) Tavasoli, E.; Guo, Y.; Kunal, P.; Grajeda, J.; Gerber, A.; Vela, J. Surface Doping Quantum Dots with Chemically Active Native Ligands: Controlling Valence without Ligand Exchange. *Chem. Mater.* **2012**, *24* (21), 4231–4241. DOI: 10.1021/cm3026957.

(63) Medek, A.; Harwood, J. S.; Frydman, L. Multiple-Quantum Magic-Angle Spinning NMR: A New Method for the Study of Quadrupolar Nuclei in Solids. *J. Am. Chem. Soc.* **1995**, *117* (51), 12779–12787. DOI: 10.1021/ja00156a015.

(64) Brown, S. P.; Wimperis, S. Two-Dimensional Multiple-Quantum MAS NMR of Quadrupolar Nuclei: A Comparison of Methods. *J. Magn. Reson.* **1997**, *128* (1), 42–61. DOI: 10.1006/jmre.1997.1217.

(65) Fabini, D. H.; Laurita, G.; Bechtel, J. S.; Stoumpos, C. C.; Evans, H. A.; Kontos, A. G.; Raptis, Y. S.; Falaras, P.; Van der Ven, A.; Kanatzidis, M. G.; Seshadri, R. Dynamic Stereochemical Activity of the Sn2+ Lone Pair in Perovskite CsSnBr3. *J. Am. Chem. Soc.* **2016**, *138* (36), 11820–11832. DOI: 10.1021/jacs.6b06287.

(66) Juhás, P.; Davis, T.; Farrow, C. L.; Billinge, S. J. L. PDFgetX3: A Rapid and Highly Automatable Program for Processing Powder Diffraction Data into Total Scattering Pair Distribution Functions. *J. Appl. Crystallogr.* **2013**, *46* (2), 560–566. DOI: 10.1107/S0021889813005190.

(67) Farrow, C. L.; Juhas, P.; Liu, J. W.; Bryndin, D.; Božin, E. S.; Bloch, J.; Proffen, T.; Billinge, S. J. L. PDFfit2 and PDFgui: Computer Programs for Studying Nanostructure in Crystals. *J. Phys. Condens. Matter* **2007**, *19* (33), 335219. DOI: 10.1088/0953-8984/19/33/335219.

(68) Harris, R. K.; Becker, E. D.; Cabral de Menezes, S. M.; Goodfellow, R.; Granger, P. NMR Nomenclature: Nuclear Spin Properties and Conventions for Chemical Shifts. IUPAC Recommendations 2001. International Union of Pure and Applied Chemistry. Physical Chemistry Division. Commission on Molecular Structure and Spectroscopy. *Magn. Reson. Chem.* **2002**, *40* (7), 489–505. DOI: 10.1002/mrc.1042.

(69) Gan, Z. Rotary Resonance Echo Double Resonance for Measuring Heteronuclear Dipolar Coupling under MAS. *J. Magn. Reson.* **2006**, *183* (2), 235–241. DOI: 10.1016/j.jmr.2006.08.014.

(70) Trebosc, J.; Hu, B.; Amoureux, J. P.; Gan, Z. Through-Space R3-HETCOR Experiments between Spin-1/2 and Half-Integer Quadrupolar Nuclei in Solid-State NMR. *J. Magn. Reson.* **2007**, *186* (2), 220–227. DOI: 10.1016/j.jmr.2007.02.015.

(71) Venkatesh, A.; Hanrahan, M. P.; Rossini, A. J. Proton Detection of MAS Solid-State NMR Spectra of Half-Integer Quadrupolar Nuclei. *Solid State Nucl. Magn. Reson.* **2017**, *84*, 171–181. DOI: 10.1016/j.ssnmr.2017.03.005.

(72) Brinkmann, A.; Kentgens, A. P. M. Proton-Selective ^{17}O–H Distance Measurements in Fast Magic–Angle-Spinning Solid-State NMR Spectroscopy for the Determination of Hydrogen Bond Lengths. *J. Am. Chem. Soc.* **2006**, *128* (46), 14758–14759. DOI: 10.1021/ja065415k.

(73) Yao, Z.; Kwak, H.-T.; Sakellariou, D.; Emsley, L.; Grandinetti, P. J. Sensitivity Enhancement of the Central Transition NMR Signal of Quadrupolar Nuclei under Magic-Angle Spinning. *Chem. Phys. Lett.* **2000**, *327* (1), 85–90. DOI: 10.1016/S0009-2614(00)00805-8.

(74) Prasad, S.; Kwak, H.-T.; Clark, T.; Grandinetti, P. J. A Simple Technique for Determining Nuclear Quadrupole Coupling Constants with RAPT Solid-State NMR Spectroscopy. *J. Am. Chem. Soc.* **2002**, *124* (18), 4964–4965. DOI: 10.1021/ja025910q.

(75) Wang, Q.; Li, Y.; Trébosc, J.; Lafon, O.; Xu, J.; Hu, B.; Feng, N.; Chen, Q.; Amoureux, J.-P.; Deng, F. Population Transfer HMQC for Half-Integer Quadrupolar Nuclei. *J. Chem. Phys.* **2015**, *142* (9), 094201. DOI: 10.1063/1.4913683.

(76) Gullion, T. Rotational-Echo, Double-Resonance NMR. In *Modern Magnetic Resonance*; Webb, G. A., Ed.; Springer Netherlands: Dordrecht, 2006; pp 713–718. DOI: 10.1007/1-4020-3910-7_89.

(77) Gan, Z. ^{13}C/^{14}N Heteronuclear Multiple-Quantum Correlation with Rotary Resonance and REDOR Dipolar Recoupling. *J. Magn. Reson.* **2007**, *184* (1), 39–43. DOI: 10.1016/j.jmr.2006.09.016.

(78) Amoureux, J.-P.; Fernandez, C. Triple, Quintuple and Higher Order Multiple Quantum MAS NMR of Quadrupolar Nuclei. *Solid State Nucl. Magn. Reson.* **1998**, *10* (4), 211–223. DOI: 10.1016/S0926-2040(97)00027-1.

(79) Chen, J.; Lin, C.; Peng, G.; Xu, F.; Luo, M.; Yang, S.; Shi, S.; Sun, Y.; Yan, T.; Li, B.; Ye, N. BaGe$_2$Pn$_2$ (Pn = P, As): Two Congruent-Melting Non-Chalcopyrite Pnictides as Mid- and Far-Infrared Nonlinear Optical Materials Exhibiting Large Second Harmonic Generation Effects. *Chem. Mater.* **2019**, *31* (24), 10170–10177. DOI: 10.1021/acs.chemmater.9b03863.

(80) Kresse, G.; Furthmüller, J. Efficient Iterative Schemes for Ab Initio Total-Energy Calculations Using a Plane-Wave Basis Set. *Phys. Rev. B* **1996**, *54* (16), 11169–11186. DOI: 10.1103/PhysRevB.54.11169.

(81) Dronskowski, R.; Bloechl, P. E. Crystal Orbital Hamilton Populations (COHP): Energy-Resolved Visualization of Chemical Bonding in Solids Based on Density-Functional Calculations. *J. Phys. Chem.* **1993**, *97* (33), 8617–8624. DOI: 10.1021/j100135a014.

(82) Becke, A. D.; Edgecombe, K. E. A Simple Measure of Electron Localization in Atomic and Molecular Systems. *J. Chem. Phys.* **1990**, *92* (9), 5397–5403. DOI: 10.1063/1.458517.

(83) Savin, A.; Jepsen, O.; Flad, J.; Andersen, O. K.; Preuss, H.; von Schnering, H. G. Electron Localization in Solid-State Structures of the Elements: The Diamond Structure. *Angew. Chem. Int. Ed. Engl.* **1992**, *31* (2), 187–188. DOI: 10.1002/anie.199201871.

(84) Savin, A.; Nesper, R.; Wengert, S.; Fässler, T. F. ELF: The Electron Localization Function. *Angew. Chem. Int. Ed. Engl.* **1997**, *36* (17), 1808–1832. DOI: 10.1002/anie.199718081.

(85) The Stuttgart Tight-Binding LMTO-ASA program, version 4.7; Andersen, O. K.; Max-Planck-Institut für Festkörperforschung: Stuttgart, Germany, 1998.

TOC